Proceedings of the
Annual Stability Conference
Structural Stability Research Council
Atlanta, Georgia, April 21-24, 2020

Geometric imperfection measurements of cold-formed steel members using a portable non-contact 3D laser scanner

Yu Xia[1], Hannah B. Blum[2]

Abstract

This paper focuses on geometric imperfection measurement for a thin-walled cold-formed steel channel section by non-contact 3D laser scanning technique. A press-braked 600S250 channel member made from a 1.8-mm thick dual phase cold-formed steel sheet was used to illustrate the methodology. The member was scanned by the Artec Leo, a hand-held non-contact scanner, and the scanned data was post-processed into a dense point cloud data. The measured imperfection data was categorized into common types of imperfections, including both global (twist, bow and camber) and local (flare and crown) imperfections. Finite element simulations of channel members under compression with different lengths were conducted with three different imperfection profiles: no imperfection, sine-shape wave imperfection, and scanned imperfection. A customized program was coded to transform the scanned 3D point cloud data into nodal coordinates of the channel's finite element mesh to represent the measured imperfections. The resulting ultimate loads and deflections were compared for the three initial assumptions of initial imperfections.

1. Introduction

Thin-walled structures, including cold-formed steel framing, are sensitive to and affected by geometric imperfections. The forming process results in geometric imperfections, and for press-braked members the manufacturing accuracy depends not only on the quality of the press brake machine but also the skill of the technician. Characterizing imperfections is crucial for the design and analysis of thin-walled structures because the strength and stiffness of members are sensitive to these initial imperfections. As a common practice, the geometric imperfection is characterized as different types, including global: bow, camber and twist, and local: flare and crown, by calculation between true and design geometry. For the characterized imperfection, many standards (ASTM C955 2018, AISI 2015, European Committee for Standardization 2018, European Committee for Standardization 2009) established limitations to control the baseline of manufacturing quality.

Previous researchers have used various methods to measure true member imperfections. Dat (Dat and Peköz 1980) designed a plan to measure both local and global imperfections for CFS members.

[1]Graduate Research Assistant, University of Wisconsin-Madison, <yxia44@wisc.edu>
[2]Assistant Professor, University of Wisconsin-Madison, <hannah.blum@wisc.edu>

Two methods using telescopic method were used for measuring long columns rested vertically or horizontally, and another method using dial gauge was used for measuring short columns. Young (Young 1997) introduced the measurement method of CFS channels by using contact displacement transducers. One of the most popular methods of geometry capture is laser measurement and it has been used in many previous researchers on this topic. Niu (Niu, Rasmussen, and Fan 2015) measured a set of back-to-back bolted double-channels by an imperfection measuring rig. For each member, the geometry data was measured cross section by cross section along the member length by a movable non-contact laser scanner. Zhao (Zhao and Schafer 2016) designed a Laser-Based Imperfection Measurement Platform to measure a series of channels and zees. The laser was fixed on a circular hollow section and this section was free to move along member longitudinal direction and free to rotate its center, where the member was placed. The scanning was also accomplished cross section by cross section. Selvaraj (Selvaraj and Madhavan 2018) designed a non-contact laser scanning equipment consisted of a laser gun and scanning arms, which allowed the scanning direction of laser gun to move and rotate freely. Traditionally, 3D laser scanning of members are conducted in a stationary rig prior to testing in the lab to characterize the initial imperfections.

This paper introduces the application of geometric imperfection measurement by a new hand-held non-contact 3D laser scanner, Artec Leo. Compared with previous studies, the hand-held scanner does not require any specific position of the member to be measured, which means the member can be placed at any location where lighting condition is satisfied, including inside a testing rig while under load. Also, it has a large range of scanning, and can therefore measure structural members of different dimensions and shapes. A press-braked channel member was used to illustrate the entire process including scanning, scanning post-processing to point cloud, point cloud post-processing to imperfection characterization. Finally, the scanned data was imported into a series of finite element models and the impact of the initial imperfection assumptions on the strength capacity of a channel column was studied and compared to columns without imperfection and with sine-shape initial imperfection.

2. Measurement setup

The hand-held 3D scanner, Artec Leo, was used in this study. It has a 3D point accuracy up to 0.1 mm and a 3D resolution up to 0.5 mm, while its 3D accuracy over 1 meter is as small as 0.03%. Its furthest range of linear field of view is 838 mm $\times$ 488 mm, and its largest angular field of view is $38.5^\circ \times 23^\circ$.

A lipped channel member formed from a 1.8 mm thick dual-phase cold-formed steel sheet was used in this study. The member was constructed by press-braking a section of steel sheet in the Sheetmetal Shop at UW-Madison. The design web depth of its outer surface was 152.4 mm, the design flange width was 63.5 mm and the design lip depth was 15.875 mm. The inside radius of corner regions was designed by Eq. 1 (in mm) (the original equation was in inch) per the Product Technical Guide (Steel Stud Manufacturers Association 2015). Therefore, the design bending radius was $2t = 3.6$ mm. The design member length was 1067 mm.

$$r = \max(381/160 - t/2, 1.5t) = 2.7 \tag{1}$$

Figure 1: Different positions of the specimen for scanning

The channel member was scanned in the Jun and Sandy Lee Wisconsin Structures and Materials Testing Laboratory at UW-Madison. The recommended working distance of the scanner was from 0.35 m to 1.2 m. The channel member could be positioned freely and no clamp or support frame was needed, therefore no deformation resulted from an external force was generated and the true deformed shape due to press-braking manufacturing was scanned. When the scanning started, the real-time fusion of the scanning was displayed on the built-in screen. The software utilized an on-screen color temperature overlay plot to indicate the quality of the scanning. For example, a bluish color indicated a poor scanning quality and this region need to be further scanned, either by adjusting the spacing between the objective member and scanner or adjusting the external environment, including improving the lighting conditions or reducing the complexity of the background by removing irrelevant objects being captured by the scanner. Some regions could not been scanned by a single scanning, for example, the surface directly touched the ground. Also, the metal surface of the member was highly reflective, and some regions near the ground showed reflections of the background, which introduced noises into the scanning. Therefore, to improve the quality of the scanning, the specimen was scanned multiple times from six different perspectives as it was positioned on the ground contacted by each of its flat surface respectively (four surfaces were parallel and the other two surfaces were perpendicular to member longitudinal direction) as shown in Fig. 1. In the scanning post-processing, the scanning from these six perspectives was able to be aligned by common geometric characteristics and merged into one final scanning. To better define the geometric characteristics, six labels were made by labeling tape on inside surface of the member before scanning, for only the member outer surface was used for geometric imperfection characterization. Two major reasons were considered to discard the member inner surface scanning. One was the spacing within the member was small and it was difficult to control the lighting condition, especially around the corner. Additionally, a uniform thickness was assumed for the channel in the finite element models, therefore the difference between the thickness of inner and outer surface was not taken into account.

3. Scanning post-processing

The scanned data from the Artec Leo was transformed to the post-processing software Artec Studio 14. The software provided several helpful operations on the scanned data, including *Erase* to remove needless data including background and inner surface of the member, *Align* to align and pair scanning from multiple perspectives, *Global Registration* to capture data across all scans,

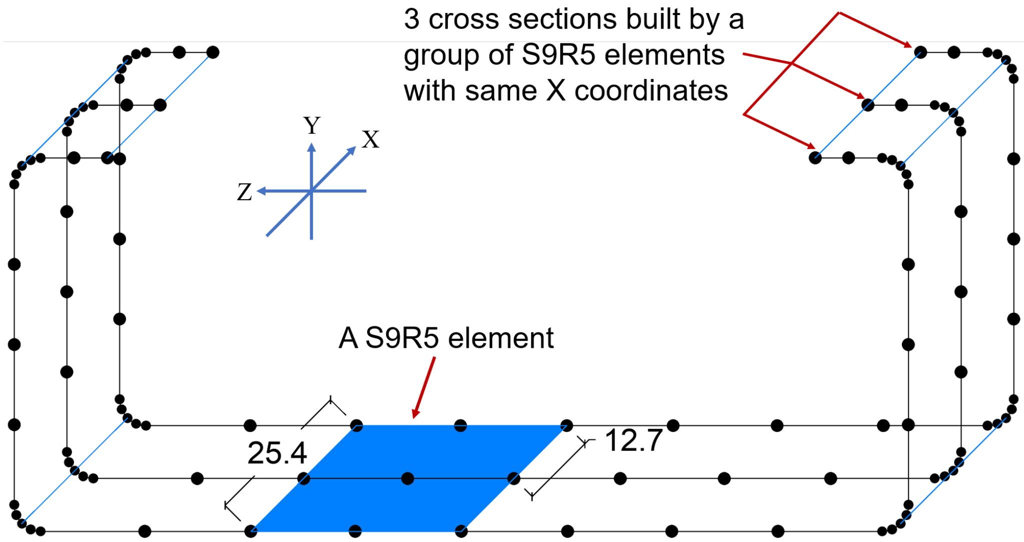

Figure 2: Relationship between nodes, S9R5 elements and cross sections (in mm)

Outlier Removal to clean up edge noise that can distort fine details, *Fusion* to fuse all the scans together into a single object, and more. After the accomplishment of all necessary operations, the post-processed scanned data was exported as point cloud data file in .asc format, which could be read by most data processing programs.

The point cloud data had a much larger data density than the demand to precisely describe the member geometry. Inspired by the idea of finite element method, a nodal mesh with design dimension of the channel member was constructed. A segment of the mesh along the longitudinal direction of the member is shown in Fig. 2. The idea to associate the point cloud data to the nodal mesh was, for each node of the mesh, to pair the corresponding scanned data by specific rule and the paired scanned data was used to depict the actual channel member geometry. A Matlab program was coded to automatically iterate node by node on each cross section and then iterate the process cross section by cross section. There were two major parts of the Matlab program. The first part *data extraction* was to extract the point cloud data points and assign them to each cross section along member length; the second part *data categorization* was to match each node on the mesh with its corresponding point cloud data.

For *data extraction*, firstly, the point cloud data was aligned with the global coordinate axes by Matlab build-in *bsxfun* function and it is shown in Fig. 3. As described in Section 2., the scanning at the member edge had a greater chance to have a relatively poor quality due to the complex lighting condition. Therefore, the point cloud data at both edges of the member was truncated 25.4 mm and the center 1016-mm segment was kept. Therefore, secondly, the desired member length, which was 1016 mm in this case, was kept by discarding data with x coordinate less than -508 mm or larger than 508 mm. Finally, the data was extracted and assigned to different cross sections by the x coordinate. The range of the x coordinate for existing data was from -508 mm to 508 mm and the distance between cross sections was 12.7 mm as shown in Fig. 2, therefore the x coordinate for cross section i is $12.7i - 520.7$ mm (1$\leq$ i $\leq$81). The x coordinate of the point cloud data was

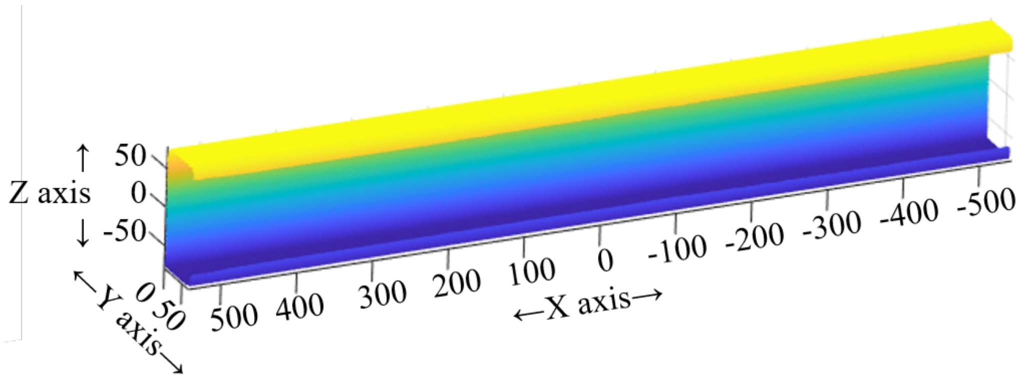

Figure 3: Scanned data plotted as 3D point cloud (in mm)

not necessarily equal to x coordinate of any cross section, therefore a tolerance of 0.508 mm was set. The scanned data with x coordinate calculated by Eq. 2 in mm was assigned to cross section i for 1< i <81; for i=1, -508 mm≤ x ≤-507.492 mm; for i=81, 507.492 mm≤ x ≤508 mm. An example of point cloud data assigned to a cross section is shown in Fig. 5.

$$12.7i - 520.954 \leq x \leq 12.7i - 520.446 \tag{2}$$

The second part *data categorization* was designed to pair the nodes of the mesh with the point cloud data. Firstly, the data within each cross section was reordered. For each cross section, a start point (e.g. point 1 in Fig. 5) was defined as the first point of the bottom lip. The next point was defined as the closest point to the current point (e.g. the start point at this moment) among the rest points. Based on this rule, all of the data was reordered. Secondly, linear interpolation was conducted between each of the two consecutive points until the distance between any of the two new consecutive points was less or equal than an assigned tolerance. In this case, a tolerance of 0.002 mm was used, which is finer than the 3D point scanning accuracy. The interpolated data was then reordered again by the same method of the first step. After that, the distance between any of the two consecutive points was generally equal, so the difference of series number between any two points was able to represent the path length between these two points. Thirdly, the flat parts (web, flanges and lips) were categorized, so that the curved parts (corners) between two consecutive flat parts were also defined. In other words, the first and the last points for each of the nine parts (two lips, two flange and one web were the five flat parts, four corners were the four curved parts) were found. To achieve this, a base line for each flat part was defined. Each cross section was generally divided into nine parts and labeled by j (j=1, 2,..., 9) as shown in Fig. 4. Five parts are flat including two lips, two flanges and one web; four parts are curved including the four corner regions. The center point for each flat part (j=1, 3, 5, 7 or 9) was found by the series number of this center point NC_j. The number of data points for lip, flange, web, or corner is calculated by Eq. 3, 4, 5 and 6 respectively.

$$n_L = \frac{(L_n - R_n) \times N}{C} \tag{3}$$

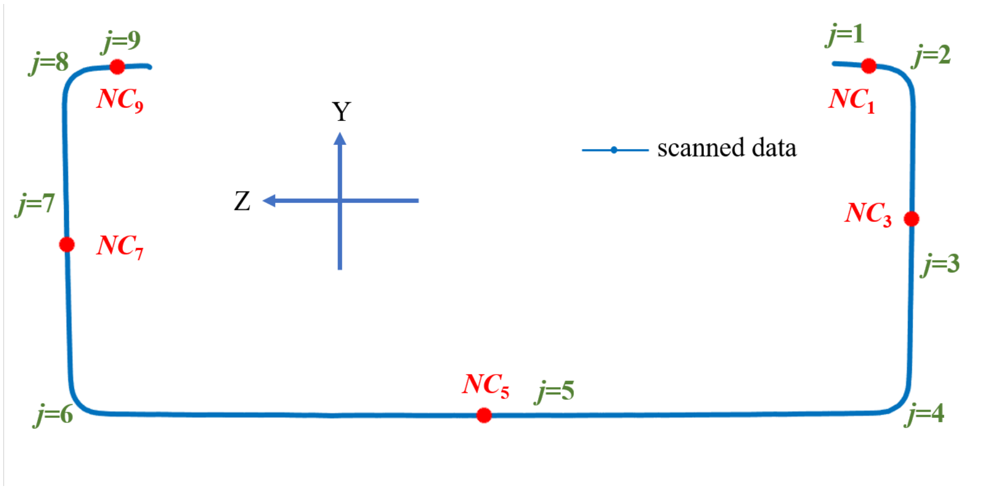

Figure 4: The point cloud data, the cross section partition and the series number for the center point of each flat part for cross section #1

$$n_F = \frac{(F_n - 2 \times R_n) \times N}{C} \tag{4}$$

$$n_W = \frac{(W_n - 2 \times R_n) \times N}{C} \tag{5}$$

$$n_R = \frac{\pi \times R_n \times N}{2 \times C} \tag{6}$$

L_n, F_n, W_n and R_n are the design dimension of lip, flange, web and corner radius; C is the perimeter of the cross section, which is calculated by adding the lengths between every two consecutive points within the cross section; N is the number of all data points in the cross section. The series number of center point NC_j for flat part j was calculated as the number of all points before flat part j plus half of the number of points for flat part j as shown in Eq. 7. *round*() stands for rounding the number within the parentheses to the nearest integer. The found center points of each flat part with their series number labelled in red font for cross section #1 is shown in Fig. 4 as an example. n_j is the number of data points for part j and it is calculated by Eq. 3 to 5. N_{j-1} is the number of data points from beginning to the end of part $j-1$ as calculated by Eq. 8. $N_0 = 0$. j=1, 3, 5, 7 or 9.

$$NC_j = N_{j-1} + \text{round}(n_j/2) \tag{7}$$

$$N_{j-1} = \text{round}(\sum_{k=1}^{j-1} n_k) \tag{8}$$

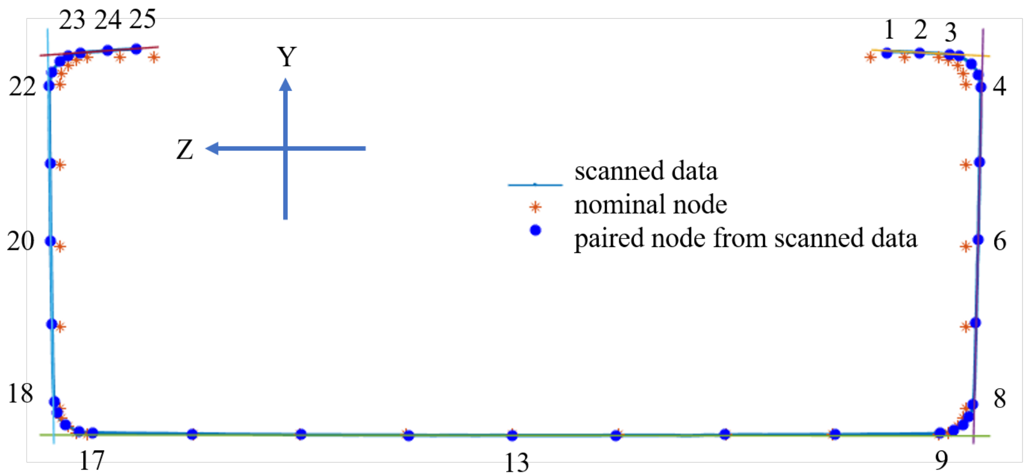

Figure 5: The point cloud data, nodes of the nodal mesh and paired nodes of the point cloud data for cross section #1

The slope of the base line for each part was calculated by linear regression between two points with series number of $NC_j \pm 0.15 \times n_j$ respectively. For each part, an iteration was built to compare the angle between two vectors by Eq. 9. The first vector v_{bl} was the unit vector of the base line, and the second vector v_{it} was formed by the center point and a variable point. For the iteration to find the first point of the flat part j, the variable point was initially selected as $NC_j - 0.15 \times n_j$ and jump one point backwards for each step of iteration; For the iteration to find the last point of the flat part j, the variable point was initially selected as $NC_j + 0.15 \times n_j$, and it jumped one point forward for each step of iteration. A tolerance of 0.3° was initialized as $\beta_{it\,\max}$. The first or the last point for each flat part was found when the angle β_{it} was equal to or larger than $\beta_{it\,\max}$. The program allowed the tolerance $\beta_{it\,\max}$ to be changed for any flat part on any cross section in case of partial low scanning quality, however this function was not required for this scanned member. For each cross section, after categorizing all flat parts and curved parts, other nodes on flat parts were paired with their counterparts of the nodal mesh by their series number. As an example of the above process, the point cloud data, nodes of the nodal mesh and paired nodes of the point cloud data for cross section #1 is shown in Fig. 5.

$$\beta_{it} = \arcsin\left(\frac{|v_{bl} \times v_{it}|}{|v_{bl}| \times |v_{it}|}\right) \tag{9}$$

The point cloud data was categorized into different types of imperfections. Both global and local imperfections were considered. For the global imperfections, twist with crown on the web, bow with crown on the web and camber on the flange were considered; for the local imperfections, flares on both flanges and crown were considered. Fig. 6 shows the situations for each considered geometric imperfections from cross section prospective. Based on the cross section discretization, the key nodes of the flat parts are labeled in Fig. 5 and were used to calculated different types of geometric imperfections. Firstly, the twist is calculated by Eq. 10, because it is not affected by the shape and the degree of the crown, but is determined by the y coordinates of web ends (point #9 and point #17). Secondly, a judgement on crown as concave or convex is made by comparison

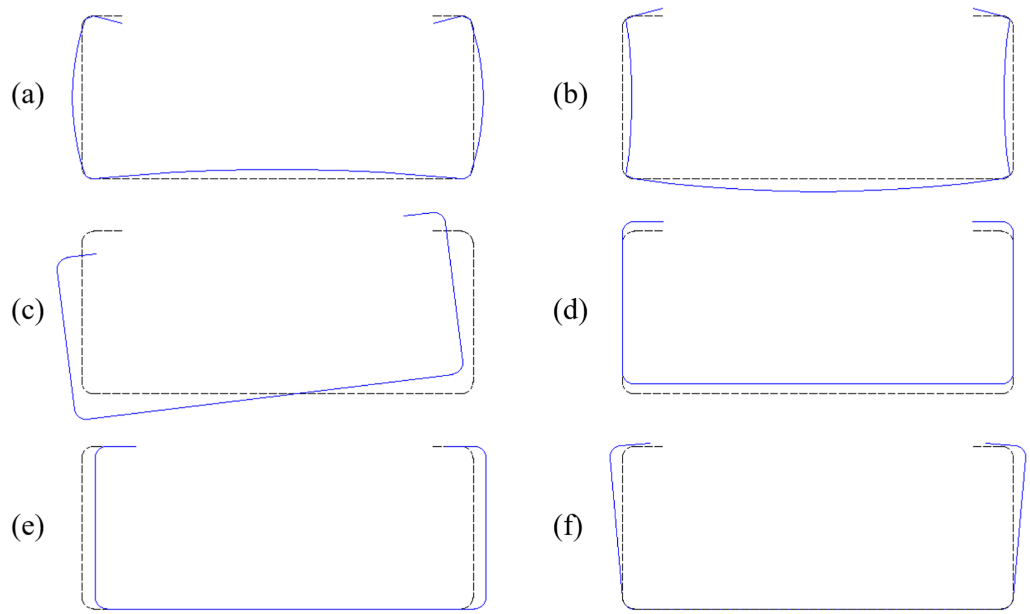

Figure 6: Geometric imperfections types from member cross section perspective: (a) concave crown; (b) convex crown; (c) twist; (d) bow; (e) camber; (f) flare

between the y coordinate of web center (point #13) and the average of y coordinates of web ends (point #9 and point #17). If the former is equal to the latter, then there is no crown for the web; if the former is larger than the latter, then the crown is concave; otherwise the crown is convex. The crown was calculated by Eq. 11, where plus sign applies to concave crown and minus sign applies to convex crown. Then, other imperfections are calculated: bow is calculated by Eq. 12, where minus sign applies to concave crown and plus sign applies to convex crown; camber is calculated by Eq. 13; flare is calculated by Eq. 14 for the bottom flange and Eq. 15 for the top flange. For above equations, Δy_i or Δz_i represents the difference of y or z coordinate between the node i on the nodal mesh and its paired node on the point cloud data, respectively. z_i represents the z coordinate of the paired node i.

$$\text{twist} = \arctan(\frac{\Delta y_{17} - \Delta y_9}{W_n - 2 \times R_n}) \tag{10}$$

$$\text{crown} = \pm(\Delta y_{13} - \frac{\Delta y_{17} + \Delta y_9}{2})/\cos(\text{twist}) \tag{11}$$

$$\text{bow} = \Delta y_{13} \pm \text{crown} \tag{12}$$

$$\text{camber} = \max\{\Delta z_8, \Delta z_{18}\} \tag{13}$$

$$\text{flare}_1 = z_{22} - z_{18} \tag{14}$$

$$\text{flare}_2 = z_8 - z_4 \tag{15}$$

A line chart of different types of imperfections along every cross sections is shown in Fig. 7. A summary of the imperfections is shown in Table 1, which includes average, coefficient of variance, standard deviation σ, minimum, minimum of absolute value, maximum and manufacturing tolerances for structural members from American and European standards. The American standard used is AISI S240-15 (AISI 2015), which is also referred by ASTM C955-18 (ASTM C955 2018). For the European standards, EN 1090-2: 2018 (European Committee for Standardization 2018) is used for global imperfections and EN 1993-1-5: 2019 (European Committee for Standardization 2009) is used for local imperfections. L represents the member length, w represents the web depth and f represents the flange width. From Fig. 7 and Table 1, twist is at a low level (ranges from 0.22° of one direction to 0.31° of the other direction) and it is stable along the member longitudinal direction for its standard deviation is as small as 0.14. The bow tended to be zero at one end and slowly increased to around 0.2 mm at 2/3 of the total length; then decreased to around -0.4 mm of the opposite direction at the other member end. The crown ranges from -0.60 mm of one direction to 0.51 mm of the other direction. From one end (cross section #1) to cross section #51, the crown is concave; from cross section #52 to the other end (cross section #81), the crown is convex. Bow is always larger than zero along member length. The average amplitude of the bow is 0.40 mm and its development is stable with a standard deviation as small as 0.09. The camber is stable along member length while the amplitude is almost always larger than 1 mm, with an average of 1.33 mm. The flare on top flange reaches its largest amplitude at two member ends with different directions, while it is close to 0 around the center of the member. For the flare on the bottom flange, it reaches its maximum amplitude at one end (cross section #1) and gradually decreases with a stable decreasing rate until its direction changes at the other end. Compared to the limitations of the standards, bow, twist, crown and flare on both flanges strictly meet the requirements for both US and European standards. For camber, its average is above the US standard and smaller than the requirement of the European standard; however, at some specific locations, neither of the standards' requirements is met.

4. Simulation of geometric imperfection

To simulate the influence on member mechanical behavior resulting from geometric imperfection, a series of post-buckling analysis were performed by Abaqus using the modified Riks method.

In addition to the scanned geometry, three different member geometric scenarios were studied. One was perfect geometry using the nodal mesh with design dimension as mentioned in Section 3. The other had a sine shape imperfection generated by ABAQUSmaker, a tool of CUFSM (Li and Schafer 2010). The sine shape imperfection was generated on web, flanges and lips along member length and its imperfection magnitude factor was 0.03. The same program used for the imperfection categorization of the point cloud data in Section 3. was also used for the sine shape geometry scenario and its line chart summary along the member length is shown in Fig. 7(b). The

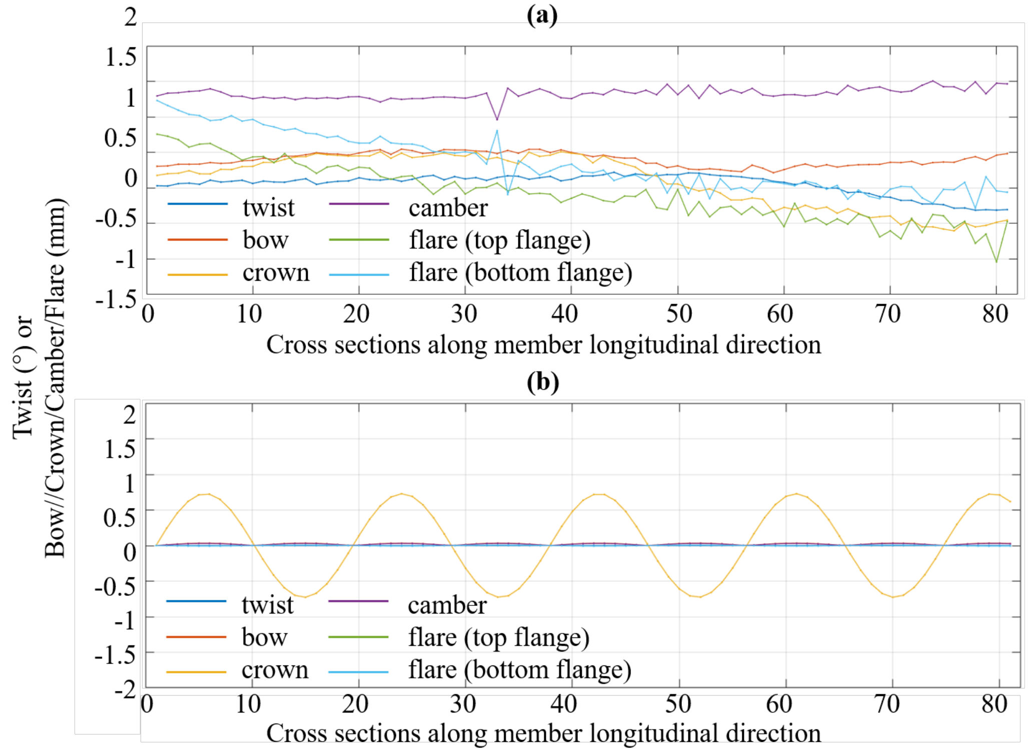

Figure 7: Categorized imperfections along member longitudinal direction for (a) scanned model (b) sine imperfection model

Table 1: Summary of categorized imperfections

#	Bow (mm)	Camber (mm)	Twist (°)	Crown (mm)	Flare (t, mm)	Flare (b, mm)
Avg	0.40	1.33	0.06	0.10	-0.08	0.35
COV	23.3%	5.91%	255%	376%	-493%	114%
σ	0.09	0.08	0.14	0.37	0.40	0.40
min	0.21	0.96	-0.31	-0.60	-1.04	-0.28
min,abs	0.21	0.96	0.0020	0.0012	0.0012	0.0063
max	0.55	1.51	0.22	0.51	0.76	1.23
US	$L/960$	$L/960$	0.0026°/mm	± 1.59	± 1.59	± 1.59
	1.11	1.11	2.77			
EN	$L/750$	$L/750$		$w/200$	$f/50$	$f/50$
	1.42	1.42		0.76	1.27	1.27

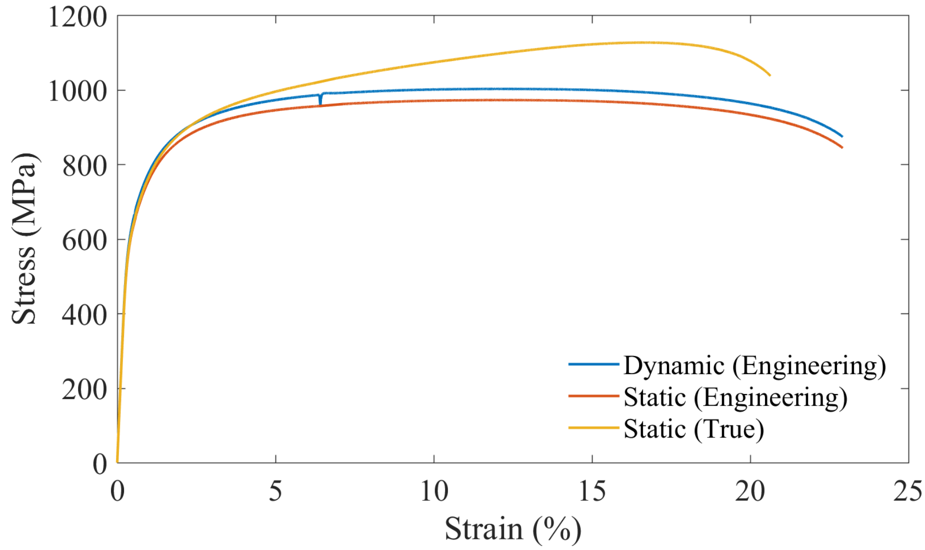

Figure 8: Stress-strain relationship of Dual Phase steel sheet

idea to determine the imperfection magnitude factor was to ensure the maximum of all types of geometric imperfections to meet the requirements for the aforementioned standards. From Fig. 7(b), the major imperfection is crown and its maximum amplitude is 0.76 mm, which is less than the limitation of US standard and equal to the limitation of European standard; other types of imperfections are minor and all are less than the limitations of aforementioned standards.

For material properties, the engineering stress-strain relationship tested by tensile coupon test using specimens cut from the same batch of Dual Phase steel sheet is shown in Fig. 8. The input stress-strain relationship in the material module of Abaqus is true stress-strain relationship and the conversion between engineering stress/strain and true stress/strain are calculated by Eq. 16 and 17.

$$\sigma_{true} = \sigma_{engineering} \times (1 + \epsilon_{engineering}) \tag{16}$$

$$\epsilon_{true} = \ln(1 + \epsilon_{engineering}) \tag{17}$$

For the boundary conditions, one end of the member was fixed to ground as it was restrained in all 6 degrees of freedom (DOFs); the other end was restrained in 5 DOFs and the only free DOF was the translation along member length. For the applied load, a set of concentrated compressive loads were equally applied on each node of the end surface and the sum of the load was 18 kN, which represented an initial compressive stress of 33.6 MPa. The setup of the Riks static step used for all three models is concluded as following: the initial arc length increment was 0.1; the minimum arc length increment was 0.01; the maximum arc length increment was 1.0; the estimated total arc length was 1. The analysis automatic termination condition was defined as a load proportionality factor equal to or larger than 20; the analysis was manually terminated when continuous negative step increment occurred. For the element creation, the nodal mesh was built with S9R5 shell elements, which have 9 nodes forming a 3 by 3 grid as shown in Fig. 2. The web, flange, and lip were discretized into four, two, and one element and their mesh sizes were 17.9 mm by 12.7 mm, 13.6 mm by 12.7 mm and 5.7 mm by 12.7 mm respectively. Each corner was discretized into two curved elements and its mesh size was 1.4 mm by 12.7 mm

After the accomplishment of the analysis, the undeformed shapes and Von Mises stress contour on the deformed shapes for the three scenarios of geometric imperfections is shown in Fig. 9. The perfect scenario and the sine imperfection scenario have similar stress distribution, while the perfect scenario has larger amplitude. The largest stress amplitude of both scenarios is observed at the web where distortional buckling occurred. For the scanned imperfection scenario, the buckling development is less obvious when it failed compared to the other two scenarios. The amplitude of the stress is also obviously smaller than the other two scenarios. The relationship between the reaction force at the fixed end and the axial deformation along member length at the free end is shown in Fig. 10. At the beginning, the perfect geometry scenario and the scanned imperfection scenario have similar member behavior up to a reaction force of around 6 kN while the member behavior of the sine imperfection scenario is weaker than the other two scenarios. The perfect geometry scenario has the largest peak load and deformation when failed; the scanned imperfection scenario has the smallest peak load and deformation when failed; while the situation for the peak load and deformation of the sine imperfection scenario are between the two other scenarios. The peak load for the perfect geometry scenario is 12.0 kN, for the sine imperfection scenario is 11.1 kN (7.5% reduction compared to perfect geometry scenario) and for the scanned imperfection scenario is 10.0 kN (16.7% reduction). All three scenarios experienced a drop in reaction force. The reaction force of the perfect scenario then experienced a rebound and continued increasing until a strong distortional buckling occurred which lead to member failure. The other two scenarios failed when they encountered the drop.

5. Conclusion

This paper introduces an alternative measurement method for thin-walled cold-formed steel members. The measurement was conducted by a non-contact portable 3D laser scanner Artec Leo. A press-braked lipped channel member made of 1.8-mm thick steel sheet was used as an example to illustrate the scanning and data post-processing procedure. The member was scanned multiple times from different perspectives and a series of post processing procedures were finished by Artec Studio 14 to generate point cloud data which stored member geometry information. A Matlab program was coded to process the point cloud data for flat and curve parts recognition on member cross section and categorize the typical different types of geometric imperfections. The characterized imperfections were compared to limits defined by both American and European standards. A series of finite element models with different initial geometric imperfections profiles were compared. The buckling situations and stress distribution at the end of each FEA are discussed and compared. The results exhibite an obvious deterioration of reaction force on member fixed end for scenarios using geometry with scanned imperfection, compared with the scenarios with sine shape imperfection and without geometric imperfection. A series of compressive member tests using members with same design dimension and similar manufacturing will be designed to verify the results from FEA.

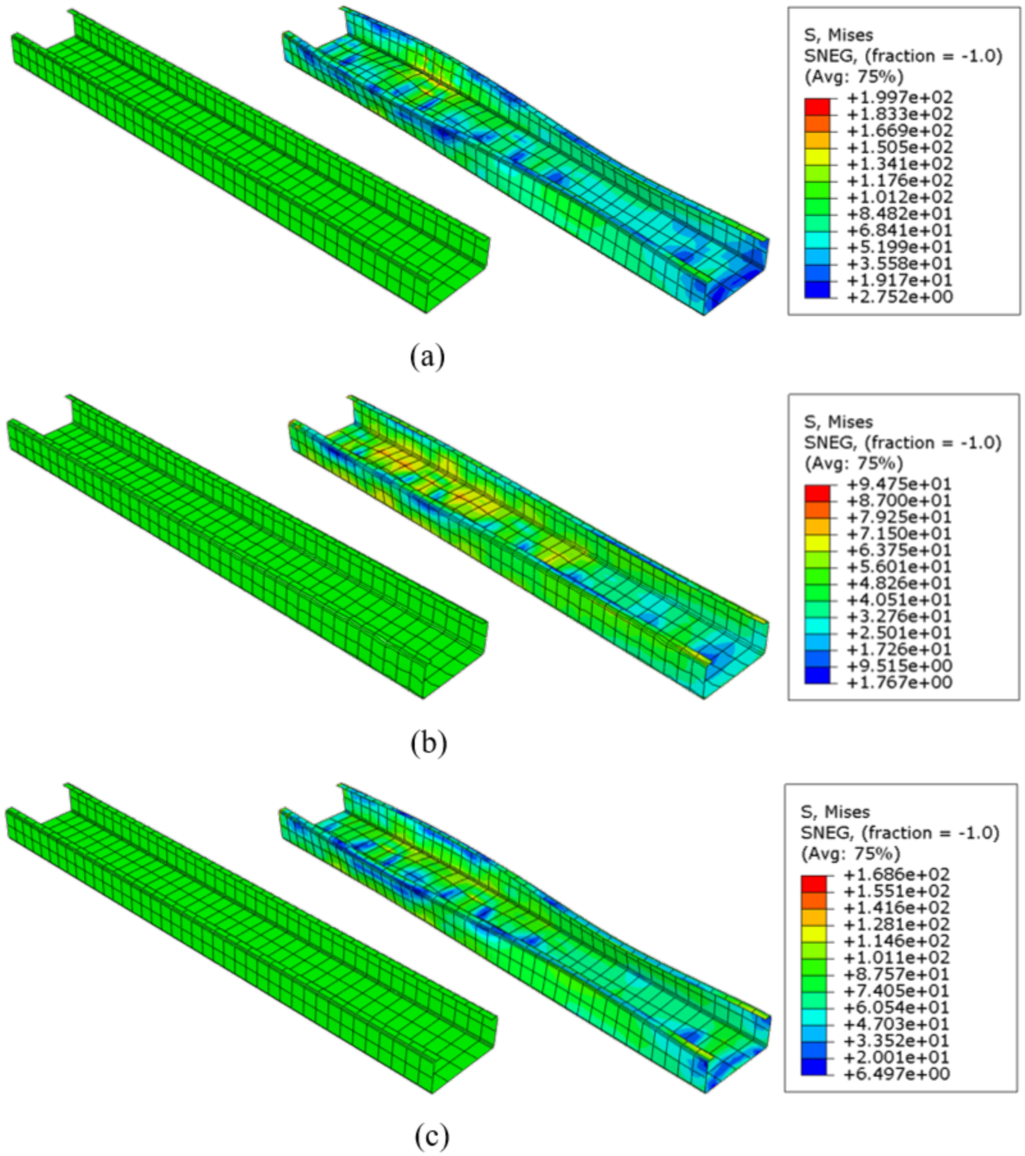

Figure 9: Undeformed shape and stress contour on deformed shape of Abaqus model for (a) perfect geometry scenario; (b) scanned imperfection scenario and (c) sine shape imperfection scenario

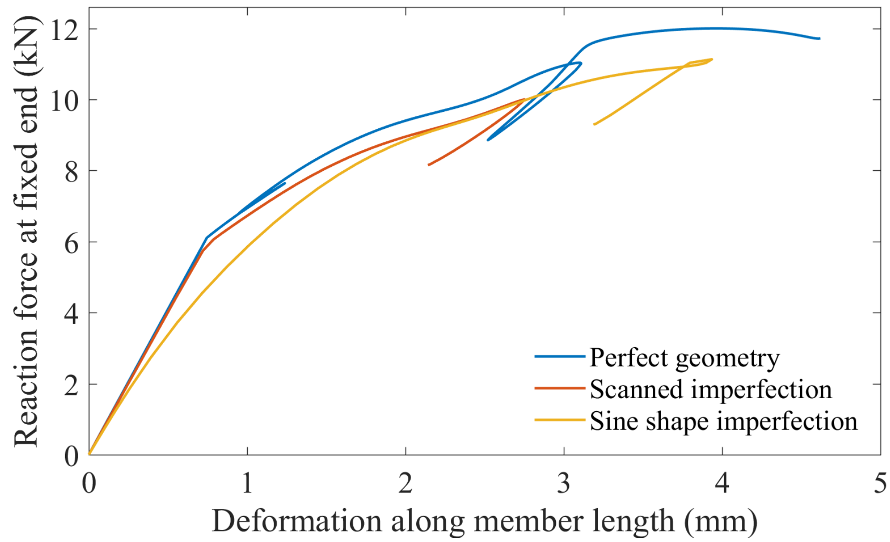

Figure 10: Relationship between deformation along member length and reaction force at fixed end for models with different geometry scenarios

6. Acknowledgements

The authors would like to thank Oliver Friis for his assistance with scanning of the member and dissemination of the software tools for preparation of post-processing during his stay as a visiting graduate research assistant.

References

AISI (2015). *North American Standard for Cold-Formed Steel Structural Framing*. Standard. AISI.

ASTM C955 (2018). *Standard Specification for Cold-Formed Steel Structural Framing Members*. Standard. ASTM.

Dat, Du Thinh and Teoman Peköz (1980). "The strength of cold-formed steel columns". PhD thesis. Cornell University.

European Committee for Standardization (2009). *Eurocode 3: Design of steel structures - Part 1-5: Plated structural elements*. Tech. rep.

— (2018). *EN 1090-2: Technical requirements for the execution of steel structures*. Tech. rep.

Li, Zhanjie and Benjamin Schafer (Nov. 2010). "Buckling analysis of cold-formed steel members with general boundary conditions using CUFSM: conventional and constrained finite strip methods". In:

Niu, Shuang, Kim Rasmussen, and Feng Fan (Aug. 2015). "Local–Global Interaction Buckling of Stainless Steel I-Beams. I: Experimental Investigation". In: *Journal of Structural Engineering* 141.8, p. 04014194. ISSN: 0733-9445. DOI: `10.1061/(ASCE)ST.1943-541X.0001137`. URL: `http://ascelibrary.org/doi/10.1061/%7B%5C%%7D28ASCE%7B%5C%%7D29ST.1943-541X.0001137`.

Selvaraj, Sivaganesh and Mahendrakumar Madhavan (Mar. 2018). "Geometric Imperfection Measurements and Validations on Cold-Formed Steel Channels Using 3D Noncontact Laser Scanner”. In: *Journal of Structural Engineering* 144.3, p. 04018010. ISSN: 0733-9445. DOI: 10.1061/(ASCE)ST.1943-541X.0001993. URL: http://ascelibrary.org/doi/10.1061/%7B%5C%%7D28ASCE%7B%5C%%7D29ST.1943-541X.0001993.

Steel Stud Manufacturers Association (2015). *Product Technical Guide*. 2015th ed. Chicago, IL: Steel Stud Manufacturers Association (SSMA), pp. 1–72. URL: http://www.ssma.com/filebin/pdf/SSMA%7B%5C_%7DProduct%7B%5C_%7DTechnical%7B%5C_%7DGuide%7B%5C_%7D11-13-17-1.3.pdf.

Young, Ben (1997). “The behaviour and design of the cold formed channel columns”. PhD thesis. The University of Sydney.

Zhao, Xi and Benjamin Schafer (Nov. 2016). “Measured geometric imperfections for Cee, Zee, and Built-up cold-formed steel members”. In: